

A generic label-free microfluidic microobject sorter using a magnetic elastic diverter

Jiachen Zhang · Onaizah Onaizah · Amir Sadri · Eric Diller

Received: date / Accepted: date

Abstract Cell sorters play important roles in biological and medical applications, such as the cellular behavior study and the disease diagnosis and therapy. This work presents a label-free microfluidic sorter that has a downstream-pointing magnetic elastic diverter. Different with most existing magnetic sorters, the proposed device does not require the target microobjects to be intrinsically magnetic or coated with magnetic particles, giving users more flexibility in sorting criteria. The diverter is wirelessly deformed by an applied magnetic field, and its deformation induces a fluid vortex that sorts incoming microobjects, e.g., cells, to the collection outlet. The diverter does not touch samples in this process, reducing the sample contamination and damage risks. This sorter uses a magnetic field generated by off-chip electromagnetic coils that are centimeters away from the device. With simple structure and no on-chip circuits or coils, this device can be integrated with other lab-on-a-chip instruments in a sealed chip, ameliorating the safety concerns in handling hazardous samples. The parallel and independent control of two such diverters on a single chip were demonstrated, showing the potential of doubling the overall throughput or forming a two-stage cascaded sorter. The sorter was modeled based on the Euler-Bernoulli beam theory and its reliability was demonstrated by achieving a raw success rate of 96.69% in sorting 1506 registered microbeads. With a simple structure, the sorter is easy and cheap to fabricate. The advantages of the proposed sorter make it a promising

multi-purpose sorting tool in both academic and industrial applications.

Keywords Microfluidic cell sorter · Magnetic actuation · Mechanical sorting · Magnetic elastic composite · Lab-on-a-chip

1 Introduction

Cell sorting is an indispensable technique for various studies and applications in cellular biology, engineering, and medicine. For example, cell sorters are extensively employed in the measurement of single cell parameters and the investigation of cellular behaviors in a culture (Mattanovich and Borth, 2006). Cell sorters minimize the interference and noise in the evaluations performed on target cells by isolating them from nontarget ones. This purification of cells not only increases the signal-to-noise ratio in subsequent analyses, but also reveals facts that are otherwise hidden (Szaniuszlo et al, 2004). Enhanced by the establishment of flow cytometry, cell sorters are now an enabling tool that becomes ubiquitous in biology and medicine relevant fields and has considerably widened our knowledge base in these areas. For instance, cell sorters are used to isolate white blood cells (WBCs) from other blood constituents in blood samples to enrich its concentration for following analyses (Nguyen et al, 2015), because the number of red blood cells (RBCs) could be one thousand times more than the quantity of WBCs and the characteristics of WBCs will be concealed by the population noise without this enrichment (Bain et al, 2011). Another application of cell sorting techniques is in the cell strain improvement. Individual cells with diverging and potential optimized cellular properties are isolated from the rest population and used to improve existing cell strains or develop new ones. In addition, cell sorting techniques

J. Zhang · O. Onaizah · E. Diller
Microrobotics Laboratory, Department of Mechanical & Industrial Engineering, University of Toronto, Toronto, Ontario, M5S 3G8, Canada.
Tel.: +1-416-978-1214
E-mail: ediller@mie.utoronto.ca

A. Sadri
Bio-Rad Laboratories (Canada) Ltd., 1329 Meyerside Drive, Mississauga, Ontario, L5T 1C9, Canada. E-mail: amir_sadri@bio-rad.com

pave the way to rare cells analysis, which is of interest in many applications.

Current commercial cell sorting platforms suffer from disadvantages such as limited sample throughput, bulky instrumentation, high cost, risks of sample contamination, and safety concerns (Shields IV et al, 2015). As a result, microfluidic cell sorters have been investigated to address these shortcomings. Existing microfluidic devices use external inputs (e.g., magnetic field (Zborowski and Chamers, 2011; Hou et al, 2011; Carr et al, 2009; Adams et al, 2008; Ramadan et al, 2006; Inglis et al, 2004), electric signal (Mazutis et al, 2013; Guo et al, 2010; Wang et al, 2007; Johann and Renaud, 2004), optical tweezer (Chen et al, 2014; Wang et al, 2011; Applegate et al, 2006; MacDonald et al, 2003), acoustic wave (Faridi et al, 2017; Li et al, 2015; Schmid et al, 2014; Ding et al, 2012), piezoelectric effect (Chen et al, 2009), and optoelectronic tweezer (Shah et al, 2009; Ohta et al, 2007; Chiou et al, 2005)), cells' properties (e.g., size (Warkiani et al, 2014; Wu et al, 2009; Russom et al, 2009; Di Carlo et al, 2007), density (Stott et al, 2010), and deformability (Hur et al, 2011; Choi et al, 2007)), or on-chip mechanical "valves"/"switches" (Yamanishi et al, 2010; Ho et al, 2005) to achieve sorting. The shared primary goal of all microfluidic cell sorters is to separate a certain group of cells from the heterogeneous mixture while all cells travel in a liquid stream within a microfluidic channel. The laminar flow nature in these channels makes it easy to focus and manipulate the cells traveling inside them. More details about the categories and advances of microfluidic cell sorters could be obtained from the reviews presented by Shields IV et al (2015) and Lenshof and Laurell (2010). Some microfluidic cell sorters have been proposed based on magnetic field, which is also a popular tool to remotely provide signals and power in other areas, such as microrobotics (Zhang et al, 2017; Zhang and Diller, 2016; Diller and Sitti, 2011; Nelson et al, 2010) and magnetic shape memory alloys (Gauthier et al, 2011). The popularity of magnetic field in actuation results from the fact that it penetrates nonmagnetic substances, including cells and polymeric materials used in cell sorters, and can generate both forces and torques simultaneously on magnetic materials.

Researchers have proposed two types of microfluidic cell sorters that rely on magnetic field. The first group of devices deal with intrinsically magnetic cells or the ones that could be bonded with magnetic particles (Hou et al, 2011; Carr et al, 2009; Adams et al, 2008; Ramadan et al, 2006; Inglis et al, 2004; Estes et al, 2009). These magnetically responsive cells are pulled by magnetic forces and separated from the nonmagnetic population. This sorting mechanism only works with a limited set of cells, and it requires additional steps to mark and unmark cells if they are not intrinsically magnetic. Nevertheless, this method allows high-throughput sorting without serial interrogations. Adams et al

(2008) demonstrated a cell sorting device that can separate two kinds of cells from the population at a throughput of 10^9 cells per hour, resulting in $> 90\%$ purity at each collection outlet after a single pass. The two kinds of cells were labeled with different superparamagnetic tags coupled to affinity reagents, while the nontarget cells were not labeled. The second group of devices use magnetic fields to activate a component within the microfluidic channel, which sorts incoming cells mechanically. These devices do not require the target cells to possess unique magnetic properties or being bonded with magnetic particles, and users can change the sorting criterion when necessary. However, these devices usually have a limited throughput because incoming cells are interrogated in series. Yamanishi et al (2010) developed a magnetized microtool that sorts incoming cells into one of the two downstream branches. The elastic microtool was deformed to divert incoming flows by magnetic fields, which were generated by electromagnetic coils beneath the device and focused to the bifurcation region.

One advantage of microfluidic sorters is that a single chip can host multiple sorters. The parallel operation of multiple sorting channels is attractive, because it could overcome the speed limitation of the devices that rely on serial processing and dramatically increase their total throughput. As one example, Lin et al (2016) proposed and demonstrated a device that was capable of simultaneous integration of eight samples.

This work proposes and characterizes a novel microfluidic microobject sorter that relies on a magnetic elastic diverter. Controlled and actuated by an externally applied magnetic field, the proposed device mechanically sorts incoming microobjects using flow vortexes induced by its diverter dynamic deformation. This magnetic sorter does not require the target microobjects to exhibit distinctive magnetic responses from the nontarget ones, and it works with various microobject sizes and shapes. Unlike many existing magnetic microfluidic sorters (Adams et al, 2008; Yamanishi et al, 2010; Ramadan et al, 2006), the proposed device does not require embedded electromagnetic coils or additional magnetic structures inside or close to the microfluidic channel, allowing it to be easily integrated with other lab-on-a-chip devices. Compared with the traditional stream-in-air sorters, the proposed device is contained on-chip and therefore more appealing for applications where safety is of concern. The facile integration of the proposed sorter with other on-chip devices opens up the possibility of sorting and analyzing samples within one sealed microfluidic device, considerably relieving the risks of sample and environment contamination of processing aerosolized or hazardous samples. The diverter does not touch incoming microobjects during sorting, reducing the risks of sample contamination and damage. The diverter only needs to move a limited distance in order to sort microobjects, making high speed sorting a pos-

sibility. A high success rate was obtained in the autonomous sorting experiment. The diverter behavior with respect to the applied magnetic field was modeled based on the Euler-Bernoulli beam theory. Theoretical predictions were then compared against experimental observations and showed a good agreement. Moreover, two diverters were demonstrated to be actuated independently and simultaneously by a single magnetic field, enabling the parallel operation for higher throughput or two-stage sorting. The unique characteristics of the proposed sorter endorse it as a promising potential tool in biological and biomedical applications.

2 Device design

The three-dimensional (3D) structure of the proposed sorter is schematically illustrated in Fig. 1(a) with the local coordinate frame. This device consists of a microfluidic bifurcation channel and a downstream-pointing magnetic elastic diverter. The sample flow, which carries incoming microobjects, is focused horizontally by two sheath flows located on its both sides, see Fig. 1(b). In addition, the V-grooves protruding from the channel ceiling and floor guide the sheath flows to focus the sample flow vertically without introducing new flow inlets or complicating other channel structures, as proposed and verified by Howell et al (2008). As a result, the incoming microobjects are focused horizontally as well as vertically into the geometric central region of the channel cross-sectional area at the y - z plane. The efficacy of this 3D focus was verified by imaging the microparticles ($1.0\ \mu\text{m}$ diameter, FluoSpheres, Molecular Probes) mixed in the sheath flows, which were activated by a laser beam with a wavelength of 407 nm. Emitted signals from these microparticles were collected by a confocal microscope (Nikon A1). Experimental observations of the sheath flow at the first V-groove, before V-grooves, and after V-grooves are shown in Fig. 1(c), which clearly show that the sample flow was focused to the channel center. Only the lower $100\ \mu\text{m}$ of the channel is shown here, because the microscope objective was located beneath the channel whose top portion could not be imaged without severe artifacts. More confocal microscopy results are available in the supplementary material.

As the most critical component in the sorter, the diverter is equally divided into a root and an arm, which nests inside one channel sidewall and hangs inside the channel, respectively. The side-view of the diverter in Fig. 1(b) shows that two rows of sawteeth exist at the top and the bottom of its arm, reducing the contact area and thus facilitate the disengagement when the diverter arm accidentally touches the channel ceiling or floor. Not pointing against the incoming flows, the diverter is stable and can deform easily regardless of the flow speed.

The 3D focus ensures incoming microobjects to circumvent the diverter tip, instead of passing through the gaps be-

tween the diverter arm and the channel walls. The sample flow position along axis y is determined by the volumetric ratio of the two sheath flows and denoted by $\eta = V_1/V_2$, where V_1 and V_2 are the volumetric rates of sheath flow 1 and 2, respectively. When $\eta = 1$, the sample flow is focused to the exact channel centerline. Setting η to be slightly smaller than 1, the focused flow is shifted towards $+y$ and all incoming microobjects go into the waste outlet, when magnetic fields are absent and the diverter remains stationary. When an incoming microobject needs to be sorted, a magnetic field is applied along $+y$ to generate magnetic torques on the diverter and deforms the diverter arm in the x - y plane. The diverter deformation induces a vortex near its tip, which displaces the microobjects in this region from their original streamlines and delivers them into the collection outlet, as illustrated in Fig. 1(d). The diverter restores its original shape after the magnetic field is removed. During the sorting, the diverter does not touch the incoming microobjects, reducing the risks of sample contamination and damage.

The sorter structure is kept simple in order to reduce the fabrication cost. The main material used by the device is polydimethylsiloxane (PDMS), which stands out from other candidates owing to its biocompatibility (Ren et al, 2001), transparency to visible lights (down to 256 nm) (Michel et al, 2001), and cost effectiveness. The magnetic elastic composite allows the diverter to deform fast and repeatedly. The bio-compatibility of this composite has been investigated in our previous work and it showed no adverse effects on living cells (Zhang et al, 2017).

3 Experimental results

3.1 Sorting demonstration

A microbead (BLPMS 20-27 μm , Cospheric) was sorted into the collection outlet to demonstrate the efficacy of the proposed sorter. The top-view frames of the sorter during this process are shown in Fig 2(a-c). The sample flow was slightly shifted so that incoming microbeads would go into the waste outlet if the diverter remained stationary. However, the bead shown here was displaced by the fluid vortex induced by the diverter deformation, which was caused by the applied magnetic field, and subsequently went into the collection outlet. The ANSYS simulation results of this sorting process are shown beneath experimental frames, with the microbead being enlarged for better visualization. The color of the path represents the instance microbead speed at that position. This demonstration is also shown alongside with its simulation results in Supplementary video 1. The sample flow and the sheath flows had volumetric rates of 0.07 mL/hr and 0.67 mL/hr (two sheath flows combined), respectively. Distilled water was used as the fluid media with Tween 20

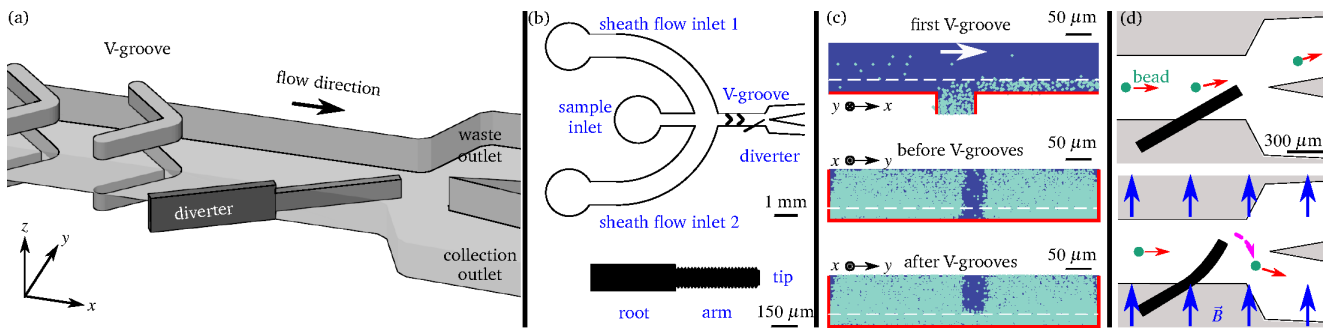


Fig. 1 Illustrations of the proposed sorter. (a) shows a 3D perspective rendering of the sorter with annotations and its local coordinate system. The sorter inlets are exhibited in the top-view drawing in (b). The diverter has a root and an arm, which has sawteeth on both its sides. Confocal microscopy results of the sorter channel are shown in (c), including a side-view (x - z plane) image at the first V-groove, and two cross-sectional (y - z plane) images before and after the two pairs of V-grooves. The white arrow points out the flow direction. Red lines mark out the channel borders, and white dashed lines denote the lower boundary of the diverter arm. Points shown here are imaged microparticles mixed in the sheath flows. The two states of the sorter, i.e., ‘idle’ and ‘active’, are presented in (d). Red arrows denote the moving directions of incoming microobjects, and the dashed arrow represents the flow vortex caused by the diverter deformation

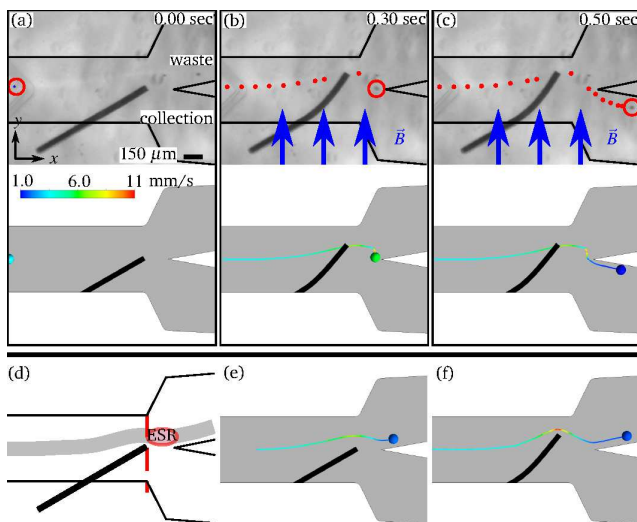


Fig. 2 A sorting demonstration and the schematics showing the working principles of the sorter. A microbead was sorted to the collection outlet, as shown in (a)-(c). The bead position at the time indicated by the time stamp in each frame is marked out by a circle, while the dots pinpoint the bead trajectory. The corresponding simulation result is shown beneath each experimental frame. The effective sorting region (ESR) is illustrated in (g). A microbead will not be sorted to the collection outlet when the diverter remains stationary, no matter whether the diverter is undeformed (e) or deformed (f). All simulation frames share the same color bar in (a)

(BioShop Canada) added to reduce the water surface tension.

As shown in this demonstration, a microobject needs to be caught by the fluid vortex created by the diverter deformation in order to be successfully sorted into the collection outlet. In other words, the microobject has to be within a specific region when the diverter deforms. This region is defined as the effective sorting region (ESR) and illustrated in Fig. 2(d). The position and size of ESR depend on the y position and x velocity of incoming microobjects, and the speed

and magnitude of the diverter deformation. In this work, the ESR is approximated as an ellipse between the diverter tip and the bifurcation point. It should be noted that the sorting is accomplished by the dynamic vortex, which disappears shortly after the diverter deformation. Without this dynamic vortex, all incoming objects will go into the waste outlet no matter whether the diverter is deformed or not, as shown in Fig. 2(e) and (f) and Supplementary video 2.

3.2 Reliable sorting performance

A computer vision-based feedback control system was built to experimentally investigate the feasibility and reliability of the proposed sorter in practical autonomous sorting tasks. As shown in Fig. 3(a), the setup consists of a syringe pump (NE-1000, New Era Pump Systems), a custom-built electromagnetic coil system, a stereo-microscope (SMZ745T, Nikon), an optical firewire camera (FO134TC, FOculus, 640×480 pixels, 60 fps), and a Linux computer. The sorter was placed on the central stage of the coil system, whose image was magnified by the microscope, captured by the top-view camera, and then delivered to the computer for image processing and algorithmic operations. More details about this coil system is available in the supplementary material. For the demonstration purpose of this sorting task, the sorter was autonomously actuated to sort incoming beads (BLPMS, diameter 20 - $27 \mu\text{m}$, Cospheric) to the two outlets alternatively, i.e., if one bead was delivered to the waste outlet, the next bead should be conveyed to the collection outlet.

To achieve the autonomous sorting, the position and velocity of each incoming bead were extracted from frames and used by the controller to predict when the bead would enter the ESR. If this bead should be sorted to the waste outlet, the sorter would not be activated, because the sample flow was shifted from the channel centerline and all in-

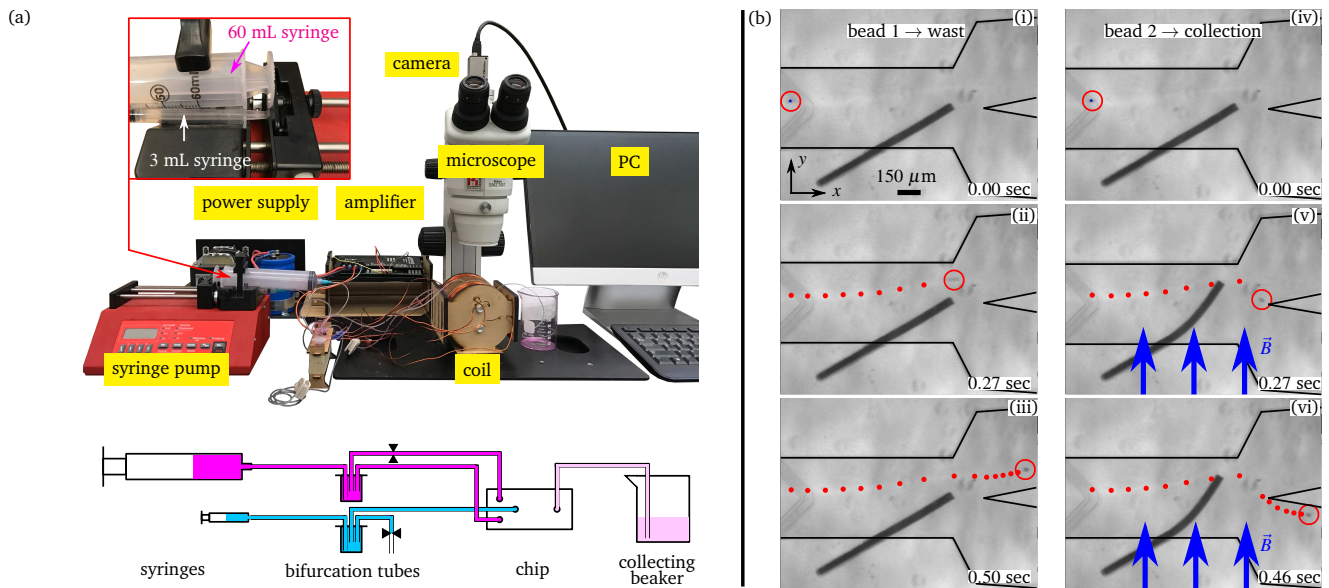


Fig. 3 Setup and results of the autonomous sorting experiment. A photograph of the setup is shown in (a) with annotations. The inset gives a closer look at the two syringes that were mounted on the same syringe pump. The flow path of this setup is schematically drawn below the picture. A bifurcation tube was used to deliver the sheath flow from the 60 mL syringe to the two sheath flow inlets of the chip. Another bifurcation tube was used to damp the sample flow. Without the second bifurcation tube, the nonideal characteristics of the syringe pump would result in a pulsing sample flow, whose width would fluctuate periodically after being focused. For the purpose of demonstration, the two downstream branches of the chip converge to one outlet, delivering all fluid into the collecting beaker. Six top-view frames captured by the camera during the experiment are shown in (b). The circle in each frame marks out the current bead position, while the dots denote the previous registered positions of the same bead. These frames show that two beads were autonomously sorted into the two downstream branches alternatively. Undeformed diverter left incoming beads undisturbed into the waste outlet, as shown in (b)(i-iii). In contrast, a diverter deformed when a bead reached the ESR displaced this bead from its original streamline into the collection outlet, as demonstrated in (b)(iv-vi). Time stamps are shown at the bottom-right corner of frames

coming beads went to the waste outlet without interferences. Otherwise, this bead needed to be collected and the controller would power currents into the coil system to generate a pulse magnetic field, which would deform the diverter at the moment when the bead entered the ESR. The bead would be captured by the vortex induced by the diverter deformation and displaced from its original streamline, which went into the waste outlet, to a new path that flowed into the collection outlet. The frames in Fig. 3(b) shows two representative beads that were automatically assigned to the waste and the collection outlets, respectively.

Through this experiment, a total of 1506 microbeads were correctly registered by the controller, and 1456 of them ended up in their designated branches, resulting in a sorting success rate of 96.68% among the detected objects. Assuming every single microbead was registered by the controller, which could be achieved using advanced image processing techniques in the future, the resultant recovery rate and purity of this experiment will be 95.52% and 98.21%, respectively. More specifically, 95.52% of the targets were successfully sorted into the collection branch, and the collection reservoir had a purity of 98.21%. Some representative successful and failed sortings in this experiment are shown in Supplementary video 1 and 2, respectively. It is noted that the beads in many failed cases had much slower velocities than average, indicating that they were located either close

to the ceiling or the floor. One possible reason is that the 3D focusing mechanism utilized by the sorter is not perfect. And a higher success rate could be expected once every incoming bead is converged to the cross-sectional center of the channel before the ESR in future research. Limited by the speed of the optical camera, the volumetric rates of the sample flow and the sheath flow were set to be 0.07 mL/hr and 0.67 mL/hr, respectively, so that the beads moved slowly enough for the camera to analyze their velocities and predict their paths in real time. In this experiment, the diverter deformed its tip up to 167 μm to sort the beads that needed to be delivered to the collection outlet. The proposed sorter obtained a relatively high success rate in this experiment even with elementary image processing techniques and imperfect 3D focusing mechanism, endorsing that the sorter is feasible as well as reliable in practical sorting applications.

4 Materials and methods

4.1 Device fabrication

The proposed sorter was fabricated using standard photolithography and mold replica techniques. Three parts of the sorter, i.e., its channel body, channel floor, and diverter, were made separately and then manually assembled together. This pro-

cess is schematically illustrated in Fig. 4. First, the contour of each part was plotted using a CAD software and defined on photomasks through a mask writer (Heidelberg μ PG 501). Then, a mold was made for each part using the following steps. Photoresist (SU-8, MicroChem) was spin coated on a silicon wafer (3 inch diameter, University Wafer) to form a film with a certain thickness value. The wafer coated with the photoresist was baked on a hot plate at 65°C and then 95°C. It was then exposed to ultraviolet (UV) lights in a mask aligner (OAI model 30). During the exposure, the corresponding mask was placed on top of the wafer to control which region of the photoresist was exposed, see Fig. 4(a-i). Afterwards, the wafer bearing the photoresist was baked again on a hot plate at 65°C and then 95°C. It was developed in a chemical solution (SU-8 Developer, MicroChem), and finally baked on a hot plate at 170°C for 10 minutes. The development process removed the section of photoresist that was covered by the mask during the exposure, leaving the cross-linked photoresist attached to the wafer to form the desired mold. The baking time and the UV exposure time were determined according to the photoresist thickness and the receipt given by the photoresist datasheet.

An additional step was inserted into the aforementioned procedure to make the mold for the channel body, because the v-grooves protrude from the channel ceiling. To make this 3D feature, the channel mold had a second layer of photoresist, while the floor mold and the sorter mold each had only one layer. After the first layer was exposed, a new layer of photoresist was spin coated on top of the first layer. The wafer bearing two layers of photoresist was then baked and exposed to UV lights through a mask with the geometry of v-grooves written on it, as shown in Fig. 4(a-ii). To align the second mask with the already exposed first layer of photoresist, a different mask aligner (EVG 620) was used instead of the one introduced before. Afterwards, the wafer with two layers of photoresist was baked at 65°C and then 95°C. It was developed in a chemical solution (SU-8 Developer, MicroChem), and then baked at 170°C. The result is a two-layer positive (protruding) photoresist mold for the channel body, see Fig. 4(a-iii). The vertical profiles of the positive mold for the channel body and the negative mold for the diverter are shown in Fig. 4(b). The channel is roughly 160 μ m thick with V-grooves protruding 70 μ m from the ceiling. The diverter mold is 40 μ m deep.

The sorter is mainly made of polydimethylsiloxane (PDMS, Sylgard 184, Dow Corning), which comes in two parts: a base polymer (part A) and a curing agent (part B). Part A and B were mixed thoroughly in a ratio of 10 : 1 by weight. One portion of the mixture was degassed in a vacuum chamber for 15 minutes, poured into the petri dishes that contained the channel body mold and the floor mold, respectively, and then degassed for another 15 minutes. Fig. 4(a-iv) shows the channel body mold as an example. The rest of the mixture

was blended with permanent magnetic particles (MQFP-15-7, NdPrFeB, Magnequench) in a ratio of 1 : 1 by weight, to make a kind of magnetic elastic composite. This composite was stirred well, degassed in a vacuum chamber for 15 minutes, poured into the negative diverter mold, and then degassed for another 15 minutes. The excess composite was scraped off by a razor blade, see Fig. 4(a-vi). Then, all molds were baked to 70°C in an oven for 5 hours to fully cure the PDMS. After curing, the diverter were taken out from the mold and magnetized using a uniform magnetic field of 1.1 T created by two permanent magnets (1 inch cube, Nd-FeB, N40, Magnet4US), see Fig. 4(c). The magnetic field strength in operations is always smaller than 20 mT, and therefore the diverter magnetization does not change in operations. The channel body and floor were collected from their respective molds and a 5/64 inch diameter punch was used to drill holes for inlets and outlets on the channel body. Finally, the diverter was manually assembled into the channel body, which was plasma bonded with the floor using a plasma etcher (Herrick Plasma Cleaner PDC-001) to form a complete device, see Fig. 4(d). The assembled device was then placed on a hot plate at 80°C for 4 hours to enhance the bonding.

4.2 Magnetic working principles

Magnetized magnetic particles are homogeneously embedded in the diverter body. When a uniform external magnetic field \mathbf{B} is applied, this decentralized allocation of particles results in distributed magnetic torques along the diverter body, see Fig. 5(a). The profile of the distributed magnetic torques is described by $\boldsymbol{\tau}(s)$ with a unit of Newton, where s is defined as a coordinate along the diverter arm. For convenience, torques that bend the diverter towards the upstream direction is designated with positive signs, and thus the scalar value of $\boldsymbol{\tau}(s)$ is

$$|\boldsymbol{\tau}(s)| = M|\mathbf{B}|\sin\alpha(s), \quad (1)$$

where α is the angle from the local magnetization to the magnetic field \mathbf{B} , as indicated in Fig. 5(a). Since the diverter root is nested inside the channel sidewall, the hanging diverter arm forms a cantilever beam scenario, i.e., it has a fixed-free boundary condition. As a result of the distributed magnetic torque $\boldsymbol{\tau}(s)$, the bending moment $Q(s)$ along the diverter arm is

$$Q(s) = \int_0^L \tau(\tilde{s})d\tilde{s} - \int_0^s \tau(\tilde{s})d\tilde{s}, \quad (2)$$

where L is the length of the bendable part of the diverter. Ideally, L should equals to 0.5 mm. However, it varies from chip to chip due to the existence of tolerances in the manual assembly of the diverter into the channel. The diverter

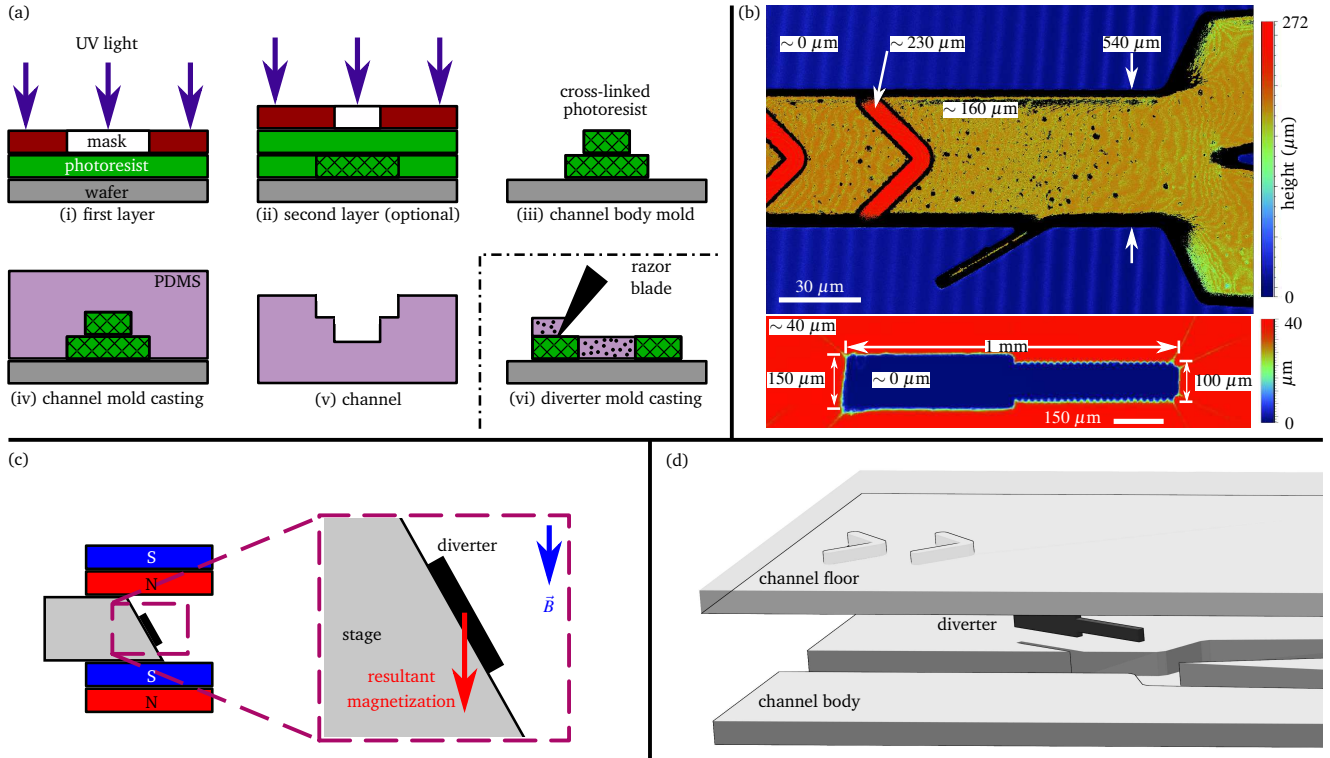


Fig. 4 Fabrication procedures of the developed sorter. Molds were made using standard one-layer or two-layer photolithography techniques, as shown in (a)(i)-(iii). Subfigure (a)(iv)-(vi) show that the channel body and the channel floor were made from the mold replica of their corresponding positive (protruding) molds, while the diverter was cured inside its negative (concave) mold. The height profiles of the channel body and the diverter molds are shown in (b). After the diverter was magnetized (c), the channel body, channel floor, and diverter were manually assembled together (d)

deforms under the bending moment $Q(s)$ and the displacement of the diverter tip is defined as h , as shown in Fig 5(b). Utilizing the Euler-Bernoulli beam theory, the curvature of the diverter arm can be related to the bending moment $Q(s)$ as

$$\kappa(s) = Q(s)(EI)^{-1}, \quad (3)$$

where E is the Young's modulus and I is the second moment of area. The curvature profile $\kappa(s)$ determines the value of the diverter tip displacement h . Equation (1-3) not only explain the actuation principles of the diverter using a magnetic field, but also provide an approach to predict the diverter deformation once the applied magnetic field is known.

In summary, the applied magnetic field \mathbf{B} generates magnetic torques $\boldsymbol{\tau}(s)$ on the diverter, causing a change in the bending moment profile $Q(s)$ along the diverter arm. The diverter arm then bends to a certain curvature $\kappa(s)$ in response to the bending moment $Q(s)$, according to the Euler-Bernoulli beam theory. The final result is that the diverter tip is displaced to certain distance h by the applied magnetic field \mathbf{B} .

5 Discussion

5.1 Characterization of diverter tip displacement

When a magnetic field \mathbf{B} is applied along a direction that is not collinear with the diverter magnetization, the diverter arm experiences magnetic torques and deforms, whose tip displacement h is determined by the direction and strength of \mathbf{B} . Once the magnetic field direction $\angle \mathbf{B}$ is known, the diverter tip displacement h under a certain magnetic field strength $|\mathbf{B}|$ could be predicted using a custom-built Matlab script based on the magnetic principles described in the preceding section. Fig. 5(a) and (b) illustrate the diverter shapes before and after its deformation caused by the application of the magnetic field \mathbf{B} , respectively. In this case, the magnetic field \mathbf{B} is applied along axis $+y$ so that it is perpendicular with the diverter magnetization that points along axis $+x$. It could be seen in Fig. 5(b) that the angle between the magnetic field \mathbf{B} and the diverter magnetization α varies with the diverter deformation to different extents at different locations along the diverter arm. According to equation (1), the magnetic torques along the diverter arm also changes correspondingly. Thus, an analytical solution of the tip displacement h with respect to the magnetic field \mathbf{B} could not be obtained. Instead, the tip displacement h under a known

magnetic field \mathbf{B} can only be calculated using an iterative numerical algorithms until a convergence is reached.

The Young's modulus E of the diverter was measured in order to simulate the diverter displacement h from first principles. A specimen sheet made of the same material with the diverter was stretched up to a strain value of 17% in a custom-built tensile test machine, during which process the elongation and corresponding force were recorded automatically. Results were processed to generate the stress-strain relationship of the material, whose slope represents its intrinsically nonlinear Young's modulus value E . The obtained nonlinear curve shows a minimum of 1.45 MPa and a maximum of 2.23 MPa. Besides, the second moment of area I of the diverter was calculated from the known dimension values of the diverter arm as $I = bh^3/12$, where $b = 100 \mu\text{m}$ and $h = 40 \mu\text{m}$ are the width and thickness of the diverter arm, respectively. The magnetic field \mathbf{B} was applied along axis $+y$ to maximize the resultant magnetic torques on the diverter at its initial state. The strength of the magnetic field $|\mathbf{B}|$ increased from 0 to 16 mT at an interval of 0.5 mT, and the tip displacement h value corresponding to each magnetic field strength \mathbf{B} was predicted by the simulation program. These simulations were executed twice with the Young's modulus set to the minimum and maximum, i.e., $E = 1.45 \text{ MPa}$ and $E = 2.23 \text{ MPa}$, respectively, and their results are plotted in Fig. 5(c).

To investigate the accuracy of the predictions made by the proposed mathematical model, an experiment was performed to measure the diverter tip displacement h in the scenarios that were configured to be the same with the ones in the simulation. Top-view frames of the diverter were captured and the tip displacement values h were extracted from these frames by calculating the distance from the diverter tip to the extended line of the diverter root. In this experiment, the diverter tip exhibited an initial displacement h_{init} of about $50 \mu\text{m}$, which could be caused by the imperfect manual assembly of the diverter into the channel sidewall. Since the initial displacement h_{init} did not originate from the applied magnetic field \mathbf{B} , it was subtracted from the measured displacement values h when the magnetic field \mathbf{B} is applied, results in a corrected displacement value $h_c = h_{\text{raw}} - h_{\text{init}}$. The values of h_c in different magnetic field settings were plotted in Fig. 5(c) together with the predictions. It is noteworthy that the main material used by the diverter, i.e., PDMS, is highly sensitive to its fabrication conditions, such as its curing temperature (Johnston et al, 2014), and its geometric dimensions, such as its thickness (Liu et al, 2009). As a result, the Young's modulus E value of the PDMS (Sylgard 184) reported in the literature spans a wide range. In this experiment, the Young's modulus E of the diverter was measured on a rectangular sheet that was not only made of the same materials with the diverter, but also was fabricated in the same batch with the diverter, to minimize potential

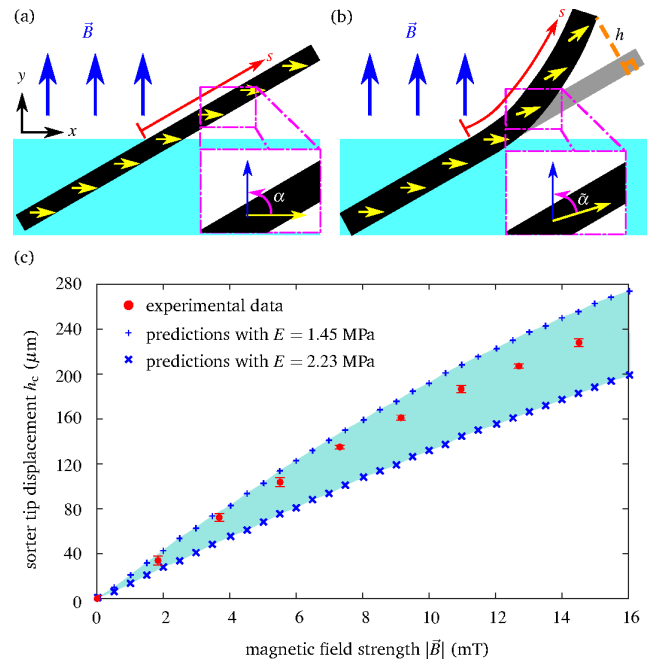


Fig. 5 Characterization of the sorter tip displacement h with respect to the applied magnetic field \mathbf{B} . The sorter arm is deformed by the magnetic torques caused by the applied magnetic field \mathbf{B} , which is applied along the perpendicular direction to the sorter magnetization, i.e., the y axis. Subfigure (a) and (b) illustrate the sorter shape in the states of prior-deformation immediately after the magnetic field \mathbf{B} is applied and past-deformation when the sorter has stopped bending, respectively. During the deformation process, the angle α between the magnetic field \mathbf{B} and the sorter magnetization varies to different extents along the sorter arm, which could be observed by a comparison between (a) and (b). The experimental observations of the sorter tip displacement h_c are plotted against the applied magnetic field strength $|\mathbf{B}|$ in (c), together with the predictions obtained using the proposed mathematical model. Each experimental data point in (c) is the average value of four measurements, and its error bar represents the standard deviation

variations in the Young's modulus E caused by inconsistent fabrication conditions. However, the Young's modulus E was measured from a tensile test, in which the sheet was uniformly stretched in a horizontal plane, while the diverter bent out-of-plane when a magnetic field is applied. Since the diverter and the test sheet underwent two distinct forms of deformation and the material itself has intrinsically nonlinear mechanical properties, the material could potentially exhibit different Young's modulus E values. In addition, the Euler-Bernoulli beam theory utilized in the proposed model has a 'small deflection' assumption, which was not satisfied in this experiment since the diverter bended a considerably large angle. Thus, the simulation results were only qualitatively compared with the experimental measurements. Nevertheless, the experimental observations fell within the region enclosed by the predicted values of the diverter tip displacement h and obeyed the trend dictated by the model, supporting the efficacy of the proposed mathematical model and magnetic principles.

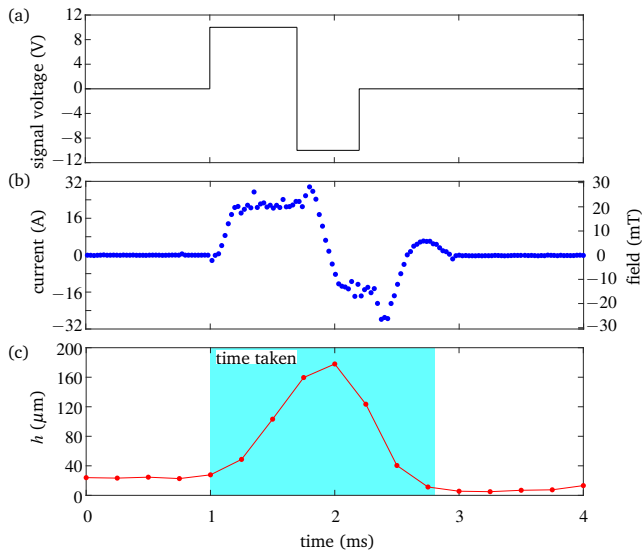


Fig. 6 Maximum deformation speed investigation of the proposed diverter using the present setup. A user specified one desired pulse signal of voltage, whose profile is shown in (a). The controller sent corresponding commands to the I/O board, which reproduced this voltage signal and delivered it to two amplifiers. Each amplifier powered corresponding currents into one coil of the electromagnetic coil system. The current profile is depicted in (b), which shares the same shape with the profile of the resultant magnetic field. The diverter deformed under the applied magnetic field, and its tip displacement is plotted in (c)

5.2 Potential sorting speed

The proposed sorter relies on the flow vortex induced by its diverter deformation to sort incoming microobjects. The diverter arm experiences a fluid drag force when it bends under the effect of an applied magnetic field. The fluid drag force impedes the diverter deformation and grows larger with the increase of the diverter deformation speed. The combined effect of the active magnetic torque and the reactive fluid drag force determines how fast the diverter arm deforms. Thus, the maximum achievable deformation speed of the diverter arm is limited by the strongest magnetic torque that could be generated by the current coil system on the diverter and the fluid drag coefficient of the fluid used.

An experiment was conducted to investigate the maximum potential sorting speed of the sorter with the current physical setup. A pulse signal was specified in the program controller, as shown in Fig. 6(a). This signal had a relatively short negative part following the positive portion to induce torques in the opposite direction that will reduce the time needed by the diverter to restore its original state. Corresponding commands were sent to the I/O board to generate this signal, which was then transferred to the input of two amplifiers. The amplifiers outputted currents that were proportional with their received inputs and provide a monitoring signal of the current output at the same time, as shown in Fig. 6(b). As a result of the coil inductance and other non-ideal parameters of the circuit, the current generated by the

amplifier had an approximately triangular shape, producing a magnetic field with the same profile. Fig. 6(c) shows that the tip displacement h of the diverter that follows the applied magnetic field to deform and restore back to its original state, finishing one sorting stroke.

As suggested by Fig. 6(c), a diverter took about 1.8 ms to finish one sorting action, including a power stroke (bends towards the upstream direction) and a recovery stroke (restores to its undeformed shape). In other words, the proposed sorter can potentially sort at a maximum of 556 Hz using the present physical setup assuming the detection mechanism can match this speed. Moreover, if a power supply and an amplifier with higher powering rating capacities are used, the maximum sorting speed of the proposed sorter can be further increased. Alternatively, the sorting speed can also be increased by optimizing the electromagnetic coil design to minimize the coil inductance without sacrificing its capability of generating strong magnetic fields. With a lower inductance, the slope in Fig. 6(b) will become steeper, the time used by the diverter to deform will decrease, and thus the overall speed of the sorter will increase. The capability of fast sorting of the proposed sorter extends the range of its potential applications in both academic and industrial areas.

5.3 Parallel operation of two sorters

One unique advantage of the proposed sorter is that its working principles allow two diverters to be independently and simultaneously controlled by a single global magnetic field. The parallel operation of two diverters could potential double the overall throughput of the sorter and therefore alleviate the speed limitation posed by the series interrogation. Owing to the fact that a global input is used instead of localized signals, the two diverters could be built in close proximity in parallel channels on the same chip or in the same channel to form a cascaded sorter. The parallel operation of two diverters are realized using the principle introduced by Zhang et al (2016), i.e., different effects can be obtained by forming distinctive angles between the magnetic field and the object magnetization vectors. The only prerequisite for this parallel operation is that the two diverters need to have different magnetization directions that are neither parallel nor antiparallel with each other.

When a magnetic field is applied along the magnetization direction of one diverter, this diverter experiences zero magnetic torque based on equation (1). At the same time, the other diverter experiences nonzero magnetic torques along its body and deforms, because its magnetization is not colinear with applied magnetic field when the prerequisite is satisfied. Thus, the two diverters are individually addressable by aligning the magnetic field with the magnetization of one diverter or the other. If the magnetic field is applied

along other directions, both diverters will deform simultaneously and their deformation angles depend on the relative angles between the magnetic field and their magnetization directions.

As a demonstration of the parallel operation capability, two diverters with magnetization angles of 10° and 97° were controlled independently and simultaneously, as illustrated in Fig. 7. As suggested by Fig. 7(b), the two diverters belong to two parallel channels that are in close proximity. Although it is not shown in preceding sections, a diverter is capable of three possible shapes: undeformed, deformed upstream, and deformed downstream, which are denoted by number 0, 1, and -1 , respectively. There are nine possible shape combinations of the two diverters, all of which were achieved by applying the magnetic field in corresponding directions. The two diverters were individually addressed when the magnetic field was along the magnetization direction of one diverter, see Fig. 7(c)-(f). When the magnetic field was along other directions, the two diverters deformed simultaneously and their deformation levels depended on the relative angles between their magnetizations and the magnetic field, as exhibited in Fig. 7(g)-(j). For the purpose of the demonstration, the two channels were not sealed and the fluidic environment was created by submerging the device under distilled water. The results presented in Fig. 7 clearly show that the two diverters can be controlled simultaneously and independently.

Being actuated by one single global magnetic field, the two diverters are operated in parallel without complicating the local chip structure to create localized signals. Other than being arranged in parallel, the two diverters can also be connected in cascade to form a two-stage sorting device to separate two different components from the same population, which will be investigated in future research. The demonstrated capability of parallel operation promises a higher throughput and the possibility of multi-target sorting.

6 Conclusions

This paper proposes and characterizes a generic label-free microfluidic microobject sorter with a downstream-pointing magnetic elastic diverter. The diverter mechanically sorts target microobjects into the collection outlet using the fluid vortex induced by its deformation. The risks of sample contamination and damage are dramatically reduced since the samples are always enclosed by the surrounding flow and experience no physical contact with the diverter. Using its mechanical sorting, the sorter is versatile and does not require the target microobjects to exhibit any distinctive magnetic responses compared with the rest of the population, allowing users to specify a variety of sorting criterion and change it whenever necessary. The diverter is deformed by

the magnetic field generated by an electromagnetic coil system, which is centimeter away from the chip. Without on-chip coils, the sorter can be integrated with other lab-on-a-chip devices into a single sealed chip, ameliorating the safety concerns involved in handling hazardous samples.

The working principles of the sorter was explained and demonstrated by both experiment and simulation results. A continuous autonomous sorting experiment showed that the sorter could perform reliable sorting with a raw success rate of 96.68%. As the most important component of the sorter, the diverter was modeled based on the Euler-Bernoulli beam theory. The relationship between the diverter deformation and the applied magnetic field was theoretically predicted and then compared against experimental observations, showing a good agreement between each other. This understanding of the sorter behavior enables further optimizations on the sorting efficacy and speed. The sorter was shown to have a potential maximum speed of 556 Hz using the current setup. A higher sorting speed could be readily achieved with more capable power supply and current amplifier instruments and electromagnetic coils with lower inductance. In addition, the capability of parallel operation of two such diverters was demonstrated, which could potentially double the overall throughput or form a two-step sorting device. This sorter is structurally simple and made of commonly available polymer materials, allowing it to be fabricated at low cost. The sorter only uses a single syringe pump to further reduce the setup cost. Different with most existing magnetic microfluidic sorters, the proposed device works with a wide range of microobjects, is versatile in sorting criteria, and has promising potentials in high-speed sorting and parallel operation. The transparency of the sorter makes it suitable for various detection strategies, such as fluorescence, laser, and visual recognition. The proposed sorter could become a multi-purpose sorting tool in various tasks involving microobject sorting, especially cell sorting, in the areas of biotechnology, microindustry, medicine, and microrobotics.

It is hoped that this work will inspire more researches on versatile multi-purpose microobject sorting devices and contribute to the advancement and diversity of this area. Future research will focus on analyzing the flow behavior inside the device and the dynamic vortex caused by the diverter deformation. Based on a better understanding of the sorter parameters, its design will be optimized, including its geometric shape and the dimension values of each part. In addition, a more advanced laser-based sample detection mechanism will be incorporated with the proposed sorter to allow it to sort at its maximum speed with a higher success rate.

Acknowledgements The authors acknowledge the use of the Centre for Microfluidic Systems in Chemistry and Biology at the University of Toronto for providing equipment access.

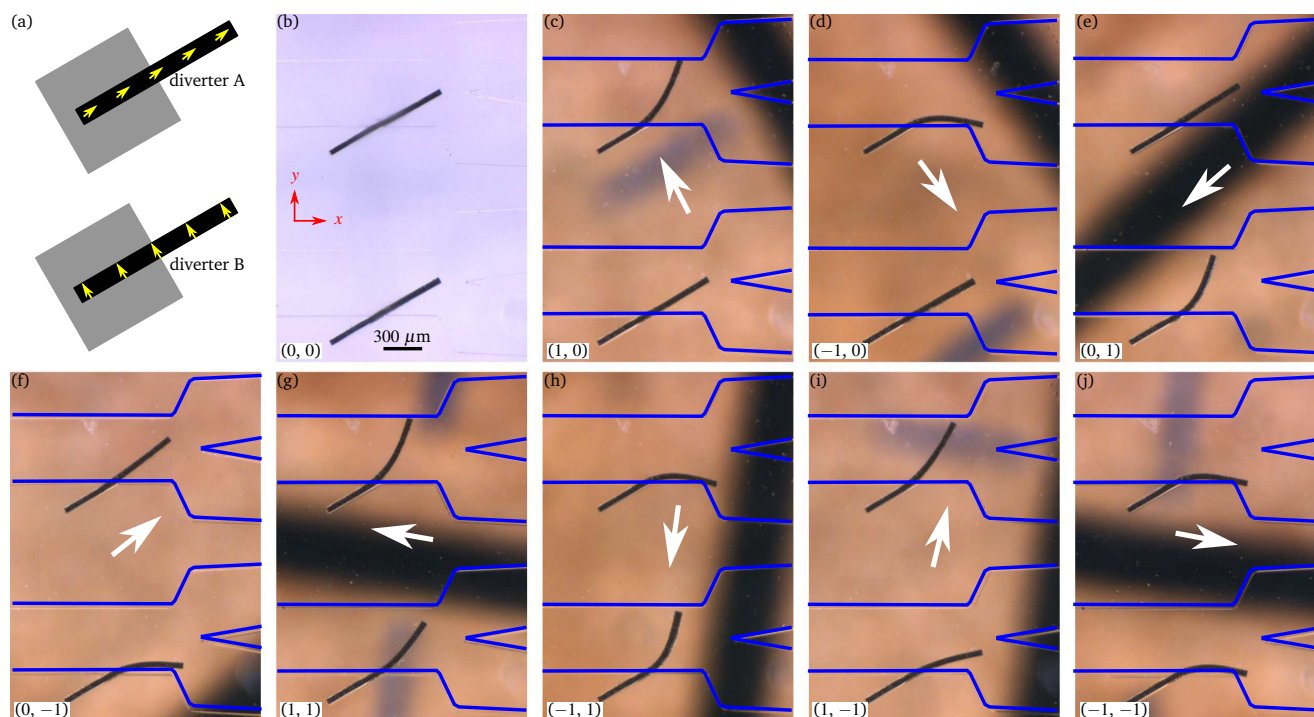


Fig. 7 Proof-of-concept demonstration of the parallel operation of two sorters. Diverter A and B were arranged side by side in two sorting channels, and their magnetization profiles are illustrated by the yellow arrows in (a). When no magnetic field was applied, the two diverters remained undeformed and a top-view photograph of this state is shown in (b) with the scalar bar. Diverter A and B were individually addressed when the magnetic field was applied along the magnetization direction of one diverter, as shown in (c-f). Alternatively, the two diverters deformed simultaneously and independently when the magnetic field was applied along other directions, as shown in (g-j). All nine possible state combinations of the two diverters were demonstrated and their corresponding state codes are marked at the left-bottom corner of each frame. The black lines in the background mark the magnetic field directions, which are also represented by the central arrows in (c-j) for better visualization. This demonstration is available in Supplementary video 3

References

- Adams JD, Kim U, Soh HT (2008) Multitarget magnetic activated cell sorter. *Proc Natl Acad Sci USA* 105(47):18,165–18,170
- Applegate RW, Squier J, Vestad T, Oakey J, Marr DWM, Bado P, Dugan Ma, Said Aa (2006) Microfluidic sorting system based on optical waveguide integration and diode laser bar trapping. *Lab Chip* 6(3):422–426
- Bain BJ, Bates I, Laffan MA, Lewis SM (2011) Dacie and Lewis Practical Haematology
- Carr C, Espy M, Nath P, Martin SL, Ward MD, Martin J (2009) Design, fabrication and demonstration of a magnetophoresis chamber with 25 output fractions. *J Magn Mater* 321(10):1440–1445
- Chen CH, Cho SH, Tsai F, Erten A, Lo YH (2009) Microfluidic cell sorter with integrated piezoelectric actuator. *Biomed Microdevices* 11(6):1223–1231
- Chen Y, Chung AJ, Wu TH, Teitell MA, Di Carlo D, Chiou PY (2014) Pulsed Laser Activated Cell Sorting with Three Dimensional Sheathless Inertial Focusing. *Small* 10(9):1746–1751
- Chiou PY, Ohta AT, Wu MC (2005) Massively parallel manipulation of single cells and microparticles using optical images. *Nature* 436(7049):370–372
- Choi S, Song S, Choi C, Park JK (2007) Continuous blood cell separation by hydrophoretic filtration. *Lab Chip* 7(11):1532–1538
- Di Carlo D, Irimia D, Tompkins RG, Toner M (2007) Continuous inertial focusing, ordering, and separation of particles in microchannels. *Proc Natl Acad Sci USA* 104(48):18,892–18,897
- Diller E, Sitti M (2011) Micro-scale mobile robotics. *Found Trends Robot* 2(3):143–259
- Ding X, Lin SCS, Kiraly B, Yue H, Li S, Chiang IK, Shi J, Benkovic SJ, Huang TJ (2012) On-chip manipulation of single microparticles, cells, and organisms using surface acoustic waves. *Proc Natl Acad Sci USA* 109(28):11,105–11,109
- Estes MD, Do J, Ahn CH (2009) On chip cell separator using magnetic bead-based enrichment and depletion of various surface markers. *Biomed Microdevices* 11(2):509–515
- Faridi MA, Ramachandraiah H, Iranmanesh I, Grishenkov D, Wiklund M, Russom A (2017) MicroBubble activated

- acoustic cell sorting. *Biomed Microdevices* 19(2):23
- Gauthier JY, Lexcelent C, Hubert A, Abadie J, Chaillet N (2011) Magneto-thermo-mechanical modeling of a Magnetic Shape Memory Alloy Ni-Mn-Ga single crystal. *Ann Solid Struct Mech* 2(1):19–31
- Guo F, Ji XH, Liu K, He RX, Zhao LB, Guo ZX, Liu W, Guo SS, Zhao XZ (2010) Droplet electric separator microfluidic device for cell sorting. *Appl Phys Lett* 96(19), DOI 10.1063/1.3360812
- Ho CT, Lin RZ, Chang HY, Liu CH (2005) Micromachined electrochemical T-switches for cell sorting applications. *Lab Chip* 5(11):1248–1258
- Hou HW, Bhagat AAS, Lee WC, Huang S, Han J, Lim CT (2011) Microfluidic devices for blood fractionation. *Micromachines* 2(3):319–343
- Howell P, Golden J, Hilliard L, Erickson J, Mott D, Ligler F (2008) Two simple and rugged designs for creating microfluidic sheath flow. *Lab Chip* 8(7):1097–1103
- Hur SC, Henderson-MacLennan NK, McCabe ERB, Di Carlo D (2011) Deformability-based cell classification and enrichment using inertial microfluidics. *Lab Chip* 11(5):912–920
- Inglis DW, Riehn R, Austin RH, Sturm JC (2004) Continuous microfluidic immunomagnetic cell separation. *Appl Phys Lett* 85(21):5093–5095
- Johann R, Renaud P (2004) A simple mechanism for reliable particle sorting in a microdevice with combined electroosmotic and pressure-driven flow. *Electrophoresis* 25(21–22):3720–3729
- Johnston ID, McCluskey DK, Tan CKL, Tracey MC (2014) Mechanical characterization of bulk Sylgard 184 for microfluidics and microengineering. *J Micromech Microeng* 24:035,017
- Lenshof A, Laurell T (2010) Continuous separation of cells and particles in microfluidic systems. *Chem Soc Rev* 39(3):1203–1217
- Li S, Ding X, Mao Z, Chen Y, Nama N, Guo F, Li P, Wang L, Cameron CE, Huang TJ (2015) Standing surface acoustic wave (SSAW)-based cell washing. *Lab Chip* 15:331–338
- Lin J, Owsley K, Bahr M, Diebold E, Carlo DD (2016) A frequency-multiplexed, microfluidic parallel flow cytometer for high-throughput screening. In: 20th International Conference on Miniaturized Systems for Chemistry and Life Sciences, pp 208–209
- Liu M, Sun J, Sun Y, Bock C, Chen Q (2009) Thickness-dependent mechanical properties of polydimethylsiloxane membranes. *J Micromech Microeng* 19(3):035,028
- MacDonald MP, Spalding GC, Dholakia K (2003) Microfluidic sorting in an optical lattice. *Nature* 426(November):421–424
- Mattanovich D, Borth N (2006) Applications of cell sorting in biotechnology. *Microb Cell Fact* 5(1):12
- Mazutis L, Gilbert J, Ung WL, Weitz DA, Griffiths AD, Heyman JA (2013) Single-cell analysis and sorting using droplet-based microfluidics. *Nat Protocols* 8(5):870–891
- Michel B, Bernard A, Bietsch A, Delamarche E, Geissler M, Juncker D, Kind H, Renault JP, Rothuizen H, Schmid H, SchmidtWinkel P, Stutz R, Wolf H (2001) Printing meets lithography: Soft approaches to high-resolution patterning (vol 45, pg 697, 2001). *IBM J Res Dev* 45(6):870
- Nelson B, Kaliakatsos I, Abbott J (2010) Microrobots for minimally invasive medicine. *Annu Rev Biomed Eng* 12:55–85
- Nguyen J, Wei Y, Zheng Y, Wang C, Sun Y (2015) On-chip sample preparation for complete blood count from raw blood. *Lab Chip* 15(6):1533–1544
- Ohta AT, Chiou PY, Han TH, Liao JC, Bhardwaj U, McCabe ERB, Yu F, Sun R, Wu MC (2007) Dynamic cell and microparticle control via optoelectronic tweezers. *J Microelectromech Syst* 16(3):491–499
- Ramadan Q, Samper V, Poenar DP, Yu C (2006) An integrated microfluidic platform for magnetic microbeads separation and confinement. *Biosens Bioelectron* 21(9):1693–1702
- Ren X, Bachman M, Sims C, Li GP, Allbritton N (2001) Electroosmotic properties of microfluidic channels composed of poly(dimethylsiloxane). *J Chromatogr B Biomed Sci App* 762(2):117–125
- Russom A, Gupta AK, Nagraath S, Carlo DD, Edd JF, Toner M (2009) Differential inertial focusing of particles in curved low-aspect-ratio microchannels. *New J Phys* 11(7):075,025
- Schmid L, Weitz Da, Franke T (2014) Sorting drops and cells with acoustics: acoustic microfluidic fluorescence-activated cell sorter. *Lab Chip* 14(19):3710–3718
- Shah GJ, Ohta AT, Chiou EPY, Wu MC, Kim CJ (2009) EWOD-driven droplet microfluidic device integrated with optoelectronic tweezers as an automated platform for cellular isolation and analysis. *Lab Chip* 9(12):1732–1739
- Shields IV C, Reyes C, López G (2015) Microfluidic cell sorting: a review of the advances in the separation of cells from debulking to rare cell isolation. *Lab Chip* 15(5):1230–1249
- Stott SL, Hsu CHCH, Tsukrov DI, Yu M, Miyamoto DT, Waltman Ba, Rothenberg SM, Shah AM, Smas ME, Korir GK, Floyd FP, Gilman AJ, Lord JB, Winokur D, Springer S, Irimia D, Nagraath S, Sequist LV, Lee RJ, Iselbacher KJ, Maheswaran S, Haber Da, Toner M (2010) Isolation of circulating tumor cells using a microvortex-generating herringbone-chip. *Proc Natl Acad Sci USA* 107(35):18,392–7
- Szaniszlo P, Wang N, Sinha M, Reece LM, Van Hook JW, Luxon Ba, Leary JF (2004) Getting the right cells to the array: Gene expression microarray analysis of cell mixtures and sorted cells. *Cytometry A* 59(May):191–202

- Wang L, Flanagan La, Monuki E, Jeon NL, Lee AP (2007) Dielectrophoresis switching with vertical side-wall electrodes for microfluidic flow cytometry. *Lab Chip* 7(9):1114–20
- Wang X, Chen S, Kong M, Wang Z, Costa K, Li R, Sun D (2011) Enhanced cell sorting and manipulation with combined optical tweezer and microfluidic chip technologies. *Lab Chip* 11:3656–3662
- Warkiani ME, Guan G, Luan KB, Lee WC, Bhagat AAS, Chaudhuri PK, Tan DSW, Lim WT, Lee SC, Chen PCY, Lim CT, Han J (2014) Slanted spiral microfluidics for the ultra-fast, label-free isolation of circulating tumor cells. *Lab Chip* 14(1):128–37
- Wu HW, Lin XZ, Hwang SM, Lee GB (2009) A microfluidic device for separation of amniotic fluid mesenchymal stem cells utilizing louver-array structures. *Biomed Microdevices* 11(6):1297–1307
- Yamanishi Y, Sakuma S, Onda K, Arai F (2010) Powerful actuation of magnetized microtools by focused magnetic field for particle sorting in a chip. *Biomed Microdevices* 12:745–752
- Zborowski M, Chamers JJ (2011) Rare Cell Separation and Analysis by Magnetic Sorting. *Anal Chem* 83(21):8050–8056
- Zhang J, Diller E (2016) Tetherless mobile micrograsping using a magnetic elastic composite material. *Smart Mater Struct* 25(11):11LT03
- Zhang J, Jain P, Diller E (2016) Independent control of two millimeter-scale soft-bodied magnetic robotic swimmers. In: *IEEE Int. Conf. Robot. Autom.*, pp 1933–38
- Zhang J, Onaizah O, Middleton K, You L, Diller E (2017) Reliable grasping of three-dimensional untethered mobile magnetic microgripper for autonomous pick-and-place. *IEEE Robot Autom Lett* 2(2):835–840